Author Manuscript

Author Manuscript

Author Manuscript

Author Manuscript

HHS Public Access

Author manuscript

Nano Lett. Author manuscript; available in PMC 2021 July 12.

Published in final edited form as:

Nano Lett. 2013 February 13; 13(2): 728–733. doi:10.1021/nl304415b.

SUPER-RESOLUTION FINGERPRINTING DETECTS CHEMICAL REACTIONS AND IDIOSYNCRASIES OF SINGLE DNA PEGBOARDS

Alexander Johnson-Buck[1], **Jeanette Nangreave**[2,3], **Do-Nyun Kim**[4], **Mark Bathe**[4], **Hao Yan**[2,3], **Nils G. Walter**[*,1]

[1]Department of Chemistry, 930 N. University Ave., University of Michigan, Ann Arbor, MI 48109-1055, USA.

[2]The Biodesign Institute, Arizona State University, Tempe, Arizona 85287, USA

[3]Department of Chemistry and Biochemistry, Arizona State University, Tempe, Arizona 85287, USA

[4]Department of Biological Engineering, MIT, Cambridge, MA 02139

Abstract

We employ the single-particle fluorescence nanoscopy technique PAINT (points accumulation for imaging in nanoscale topography) using site-specific DNA probes to acquire two-dimensional density maps of specific features patterned on nanoscale DNA origami pegboards. We show that PAINT has a localization accuracy of ~10 nm that is sufficient to reliably distinguish dense (>10^4 features μm^{-2}) sub-100-nm patterns of oligonucleotide features. We employ two-color PAINT to follow enzyme-catalyzed modification of features on individual origami, and to show that single nano-pegboards exhibit stable, spatially heterogeneous probe-binding patterns, or "fingerprints." Finally, we present experimental and modeling evidence suggesting that these fingerprints may arise from feature spacing variations that locally modulate the probe binding kinetics. Our study highlights the power of fluorescence nanoscopy to perform quality control on individual soft nanodevices that interact with and position reagents in solution.

Graphical Abstract

* nwalter@umich.edu.

The authors declare no competing financial interest.

Author Manuscript Author Manuscript Author Manuscript Author Manuscript

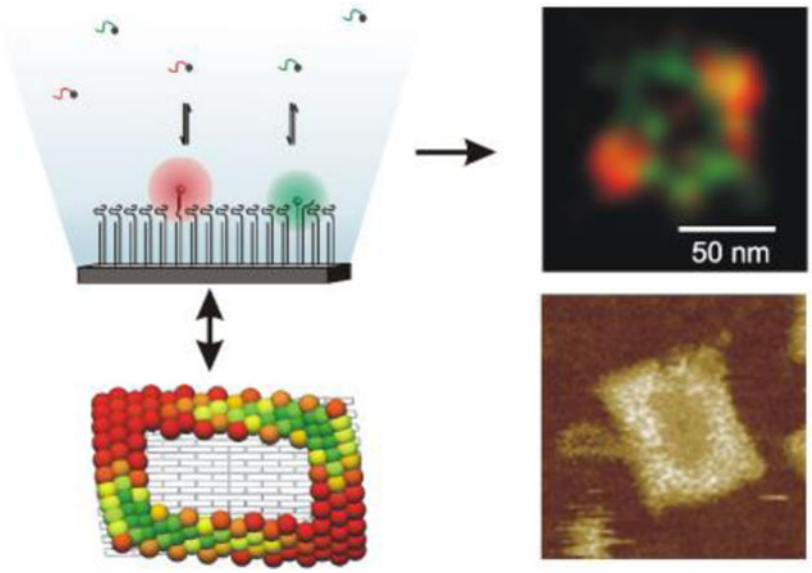

Keywords

Chemical imaging; DNA origami; PAINT; points accumulation for imaging in nanoscale topography; single molecule super-resolution fluorescence microscopy

DNA nanotechnology[1-4] has laid the foundation for a multitude of nanoscale devices that permit control over dynamic chemical or optoelectronic processes[5-10]. Many of these devices are chemically heterogeneous and labile, incorporating flexible biological components that are often closely spaced. While techniques such as atomic force microscopy (AFM) and transmission electron microscopy (TEM) yield detailed topological maps of such devices, they can damage biological samples over time and possess limited chemical specificity. As a result, AFM and TEM provide incomplete information about compositionally complex and dynamic nanodevices. Alternatively, functional characterization of DNA-based nanoscale devices is often carried out in bulk[6,8,9,11-13], potentially masking variations in performance between individual copies of a device, or within different regions of a single device.

Nanoscale fluorescence microscopy (or short, nanoscopy[14-19]) has recently advanced to combine high spatial resolution and tunable chemical specificity with relatively low invasiveness, and therefore holds promise for the spatiotemporal imaging and quality control of functional nanomaterials[10,15,17,18,20,21]. This body of techniques uses spatially confined illumination schemes[22,23] or repeated sparse sampling of features using single molecule emitters[14,24,25] to achieve resolutions well below the classical optical diffraction limit. It was recently shown that the super-resolution technique PAINT (points accumulation for imaging in nanoscale topography)[14] can be used to measure the position and hybridization kinetics of specific, spatially isolated features on DNA scaffolds[15]. In the present work, we show that PAINT can map the position and accessibility of specific single-stranded DNA (ssDNA) features in the context of very dense nanoscale arrays with spacings of only ~5 nm between adjacent features. We further use two-color PAINT to spatiotemporally monitor enzymatic

Author Manuscript Author Manuscript Author Manuscript Author Manuscript

modification of the ssDNA features, demonstrating the ability to visualize chemical changes on individual nanostructures. Finally, combining results from two-color PAINT with those from the finite-element model CanDo[26], we present evidence that local variations in the DNA tile conformation and density of ssDNA features can result in spatially heterogeneous binding properties that would escape detection by other imaging techniques.

As targets for fluorescence nanoscopy, 60 x 90 nm rectangular DNA origami tiles[1] were synthesized, each bearing 42 or 126 identical single-stranded overhangs for the attachment of substrate (**S**) oligonucleotides *via* a 20-base-pair DNA duplex (Figure 1a-d, Figure S1, Table S1). In addition, each tile had 4-5 overhangs bearing biotins on the face opposite to that of **S** for immobilization of the tiles in random orientations (Figure S2) on a NeutrAvidin-coated microscope slide (Figure 1c). Upon saturation with excess **S** (Figure S3), the tiles were immobilized on a microscope slide at a density of ~0.1 μm^{-2} and imaged on a total internal reflection fluorescence (TIRF) microscope in the presence of one or two probe strands, **α** and/or **β** (Figure 1c-d, Figure S4). Each probe was labeled at its 5′-end with a fluorophore (Cy3 or Cy5) to permit its detection upon transient binding to the DNA origami within the evanescent field of excitation light. The concentration of probes was adjusted to an optimal range of 10-20 nM so that, in general, only zero or one copy of each probe was bound to a given origami at a time (Figure 1e). This ensures accurate localization of individual binding sites, as opposed to averaged locations of multiple sites, and minimizes competition between probes (Figure 1d). We found that **α** and **β** dissociate from origami-bound **S** with rate constants of 0.34 ± 0.01 and 0.22 ± 0.03 s^{-1}, respectively (Table S2).

In each experiment, the tiles were imaged for up to 66 min, yielding 20-300 binding events per tile. The fluorescence emission profile from each probe was fit with a 2D Gaussian function to localize the probe (Figure 1f). Intensity thresholding, aided by Hidden Markov modeling, was used to select intervals in which only one probe was bound (Figure 1e). Finally, a super-resolution reconstruction was generated in which each localization was represented as a Gaussian distribution with x and y standard deviations calculated based on photon count and other imaging parameters[27], with a typical value of σ = 5-10 nm. (We found it essential to correct for microscope stage drift and to account for the impact of sampling density on the reconstruction quality; see Supporting Methods, Figures S5-S6.) These reconstructions show a dramatic improvement in resolution over the corresponding diffraction-limited images (compare Figure 1f,h).

To examine the ability of PAINT to discern different spatial arrangements of target, tiles bearing two patterns of **S** were synthesized: an open rectangle, **R** (Figure 1a), and a straight line, **L** (Figure 1b). Both patterns were imaged under identical conditions, resulting in only a few dozen localizations per origami on average. Despite the sparse sampling (Figure S6a,b), the resulting PAINT reconstructions revealed binding patterns reflecting the design (Figure 2a-b) and permitted correct identification of **R** and **L** in a blind experiment (Figure 2c). For both patterns, a significant fraction (~33% for **L**, ~50% for **R**) of reconstructions could not be classified as linear or rectangular, in agreement with independent estimates of assembly yield from AFM images (Table S3). Furthermore, a model-free alignment of 198 reconstructions of **R** origami, each comprising a larger number of 100-300 localizations (Figure S7), using standard single particle analysis software EMAN revealed several class

Author Manuscript Author Manuscript Author Manuscript Author Manuscript

averages resembling the desired rectangular structure (45-55% of origami), with most of the remaining class averages resembling aggregated or incompletely assembled origami. Many defects revealed in the PAINT images have counterparts in AFM images (Figure S7), suggesting that they are due to imperfect tile or pegboard assembly. This is consistent with the fact that the number of binding events per origami is distributed more broadly than would be predicted for binding to a set of identical, fully assembled pegboards (Figure S8). We note, however, that PAINT monitors the single-stranded DNA regions involved in interactions with external reagents that are too soft to be visible by AFM.

To demonstrate sequence-specific imaging, the **R** pattern was evaluated simultaneously in the presence of **α-Cy3** and **β-Cy5**. The resulting binding patterns were reconstructed and registered in the same coordinate space, resulting in a two-color overlay (Figure 3b, Figure S9). Unlike other fluorescence nanoscopy techniques, PAINT is insensitive to photobleaching and labeling efficiency due to the vast reserve of probes in solution that are readily exchanged for origami-bound probes, enabling stable imaging over hours. Since **S** contains a single ribonucleotide (Figure 1d), it can be site-specifically cleaved by an **8-17** DNAzyme in the presence of Zn^{2+} such that, after cleavage, the **β-Cy5** binding frequency is expected to diminish relative to that of **α-Cy3**. Incubation with the deoxyribozyme results in a time-dependent decrease in **β-Cy5** relative to **α-Cy3** binding, consistent with but going beyond ensemble-averaged measurements (Figure 3b-c, Figure S3) by demonstrating PAINT's ability to spatiotemporally monitor enzymatic remodeling reactions on individual origami nanodevices.

The use of two probe strands also provides a means of assessing the homogeneity of binding to nanostructures. Surprisingly, we found several cases where one probe bound uniformly across the pattern of **S** and the other did not, even for well-formed **R** patterns (Figure 4a). To rule out fluorophore-specific imaging errors as the source of non-uniform binding, a set of **R** origami was imaged first with the probe combination **α-Cy3** + **β-Cy5** and subsequently with the labels inverted, i.e., **β-Cy3** + **α-Cy5**. A chi-squared test of homogeneity across different quadrants of the rectangular pattern (Figure S9) revealed that the binding patterns of **α-Cy3** and **α-Cy5** to the origami in Figure 3 are indistinguishable from homogeneous binding, while the binding of **β-Cy5** and **β-Cy3** cannot be explained by a homogeneous model ($\chi^2(3,N>99) > 15$, $P < 0.002$). Furthermore, the intensity difference profile, calculated by subtracting the Cy5 reconstruction from the Cy3 reconstruction (Figure S10), appears to invert upon switching the probe labels (Figure 3b,c), with a 2-dimensional correlation coefficient of −0.67. Taken together, these observations suggest a "fingerprint" of sequence-specific binding patterns for this tile, with more heterogeneous binding of **β** than **α**, and that this fingerprint persists throughout the ~1 h time lag between imaging with **α-Cy3** + **β-Cy5** and **β-Cy3** + **α-Cy5**.

To determine how prevalent heterogeneous binding is within a population of **R** origami, we compared the observed distribution of χ^2 for 173 origami to the theoretical distribution from 1,000 simulated origami (Figure 4 d). For both **α** and **β**, χ^2 is skewed towards larger values than predicted from homogeneous binding, which is consistent with the observed incomplete and variable assembly of a significant fraction of the **S** patterns as noted in the yield estimates by AFM (Table S3 and Figure S11). However, the binding of **β** is more

Author Manuscript Author Manuscript Author Manuscript Author Manuscript

heterogeneous than that of **α**, a fact that cannot be explained by assembly yield alone and is not detectable by AFM imaging. To further characterize the sequence dependence and stability of binding distributions, the 2-D correlation coefficient between difference profiles with the two inversely labeled sets of PAINT probes (as in Figure 4 b,c) was calculated for 70 origami and compared to the values expected from 1,000 simulated origami (Figure 4 e). The distributions are broadened by limited sampling, but there is a bias towards negative correlation coefficients in the experimental set, indicating a sequence-specific heterogeneity of binding that persists for at least 1 h. Importantly, these patterns cannot be trivially attributed to a fraction of pre-cleaved **S**, which would lack the **β**-binding sequence (Figure S12). Furthermore, binding heterogeneity is not significantly correlated with the total number of binding events (Figure S8), which implies that some well-assembled origami with intact **S** nevertheless bind probes unevenly. Together, these data suggest that the accessibility of **β**-binding sequence varies across the surface of the origami somewhat independently of the accessibility of **α**-binding sequence.

We therefore hypothesized that local interactions between adjacent **S** strands exert a differential influence on **α** and **β** binding. To test this possibility, we measured the kinetics of **α-Cy3** and **β-Cy5** binding to origami with spacings of ~5, 10, or 20 nm between nearest-neighbor **S** strands (Figure S13). We found that **β-Cy5** binding is slowed by ~25% relative to that of **α-Cy3** at a spacing of 5 nm between **S** strands, but not 10 or 20 nm (Figure 5a). This is consistent with a model in which interactions between nearby **S** strands compete with **β** binding, inhibiting rather than enhancing its binding relative to **α** (Figure S14). Thus, if the spacing of **S** varies across the surface of a tile, there may be regions in which **β-Cy5** binding is inhibited relative to that of **α-Cy3**, resulting in heterogeneous binding fingerprints such as those in Figure 4.

A variety of factors could produce variation in **S** spacing across the surface of an origami array, including global bend/twist or distortion of the origami tile[26,28,29] and incomplete tile or staple assembly. To investigate the possible impact of tile distortion on **S** spacing, we used the finite-element model CanDo (see Supporting Methods) to predict the three-dimensional solution conformation of the **R** origami tile, accounting for constraints imposed by surface immobilization *via* biotin. The model predicts a saddle-like conformation with significant curvature (Figures 5b, S15), consistent with previous reports[26,28,29]. Using a simple model of free **S** as a flexible, freely jointed chain with root-mean-square end-to-end distance of 3.6 nm connected to the origami surface by a rigid double-stranded DNA rod of ~7-nm length (see Supporting Methods, Figure S16), the effective local concentration of **S** is predicted to vary 2- to 4-fold between different corners of the tile (Figures 5c, S16). These predictions are consistent with binding patterns observed in PAINT reconstructions (Figure S17) and a competitive inhibition model in which nearest-neighbor strands interact via non-canonical or nonspecific binding interactions that are enhanced or diminished by structurally-induced changes in inter-strand proximity. Relaxation of the position restraints at the biotin positions predicts less pronounced curvature at the corners (Figure S15b) and consequently less variation in **S** concentration across the tile (Figure S16c), suggesting that the number and orientation of surface-bound biotins can influence local variations in **S** spacing. Furthermore, since both PAINT (Figure S8) and AFM (Figure S11, Table S3) images show

Author Manuscript Author Manuscript Author Manuscript Author Manuscript

evidence of incomplete tile assembly, it is also possible that variations in assembly play a role in generating the fingerprints observed (Figure S10), as structural defects could also generate local variations in spacing between **S** strands.

Previous studies have presented mixed evidence for spatially-dependent oligonucleotide binding to origami, with a slight (10-40%) preference for binding towards the outer edges[4,15]. Our findings further show that individual origami tiles bearing dense arrays of targets can have stable fingerprints of sequence-specific interactions, with binding kinetics varying as much as twofold between different corners or edges of the tile (Figure 4 b,c,e). **S** has little self-complementarity (Figure 1d), but the locally high concentration (~2-8 mM by our model) of **S** may lead to non-Watson-Crick interactions such as G-tetrads[23] between neighboring **S** strands that, even if transient, may compete with probe binding in a sequence-specific fashion.

In summary, we employed multicolor PAINT to acquire detailed 2D maps of chemical properties of individual DNA origami tiles, revealing their previously unobservable, stable, idiosyncratic fingerprints of interaction with reagents in solution. In addition, we have shown that the low invasiveness and insensitivity to photobleaching make PAINT suitable for spatiotemporal monitoring of subtle chemical modifications to individual nanostructures. Since it reveals previously hidden properties of non-rigid features of DNA origami that can be functionalized but yield little contrast for AFM and electron microscopy, PAINT complements these more established analytical tools. PAINT should thus find broad application in the characterization of the growing toolkit of soft, internally complex, nanoscale devices with applications in fields as diverse as organic synthesis, optoelectronics and molecular robotics[10,31,32].

Supplementary Material

Refer to Web version on PubMed Central for supplementary material.

Acknowledgements

This work was partially funded by the National Science Foundation (NSF) Collaborative Research award EMT/MISC CCF-0829579 and the Department of Defense MURI award W911NF-12-1-0420. A.J.B. acknowledges support from a Rackham Predoctoral Fellowship. The authors acknowledge Georgios Skiniotis and Jeffrey Herbstman for their assistance with the EMAN alignment software, and Shuoxing Jiang and Yang Yang for their assistance with sample preparation and AFM imaging.

References

(1). Rothemund PWK Nature 2006, 440, 297–302. [PubMed: 16541064]
(2). Han D; Pal S; Nangreave J; Deng Z; Liu Y; Yan H Science 2011, 332, 342–346. [PubMed: 21493857]
(3). Pinheiro AV; Han D; Shih WM; Yan H Nat. Nanotechnol 2011, 6, 763–772. [PubMed: 22056726]
(4). Ke Y; Lindsay S; Chang Y; Liu Y; Yan H Science 2008, 319, 180–183. [PubMed: 18187649]
(5). Gu H; Chao J; Xiao S-J; Seeman NC Nature 465, 202–205. [PubMed: 20463734]
(6). He Y; Liu DR Nat. Nanotechnol 2010, 5, 778–782. [PubMed: 20935654]
(7). Maune HT; Han S; Barish RD; Bockrath M; Iii WAG; Rothemund PWK; Winfree E Nat. Nanotechnol 2009, 5, 61–66. [PubMed: 19898497]

Author Manuscript Author Manuscript Author Manuscript Author Manuscript

(8). Douglas SM; Bachelet I; Church GM Science 2012, 335, 831–834. [PubMed: 22344439]
(9). Kuzyk A; Schreiber R; Fan Z; Pardatscher G; Roller E-M; Högele A; Simmel FC; Govorov AO; Liedl T Nature 2012, 483, 311–314. [PubMed: 22422265]
(10). Lund K; Manzo AJ; Dabby N; Michelotti N; Johnson-Buck A; Nangreave J; Taylor S; Pei R; Stojanovic MN; Walter NG; Winfree E; Yan H Nature 465, 206–210. [PubMed: 20463735]
(11). Tian Y; He Y; Chen Y; Yin P; Mao C Angew. Chem., Int. Ed 2005, 44, 4355–4358.
(12). Wickham SFJ; Bath J; Katsuda Y; Endo M; Hidaka K; Sugiyama H; Turberfield AJ Nat. Nanotechnol 2012, 7, 169–173. [PubMed: 22266636]
(13). Fu J; Liu M; Liu Y; Woodbury NW; Yan HJ Am. Chem. Soc 2012, 134, 5516–5519.
(14). Sharonov A; Hochstrasser RM Proc. Natl. Acad. Sci. U.S.A 2006, 103, 18911–18916. [PubMed: 17142314]
(15). Jungmann R; Steinhauer C; Scheible M; Kuzyk A; Tinnefeld P; Simmel FC Nano Lett. 2010, 10, 4756–4761. [PubMed: 20957983]
(16). Walter NG; Huang C-Y; Manzo AJ; Sobhy MA Nat. Methods 2008, 5, 475–489. [PubMed: 18511916]
(17). Zhou X; Andoy NM; Liu G; Choudhary E; Han K-S; Shen H; Chen P Nat. Nanotechnol 2012, 7, 237–241. [PubMed: 22343380]
(18). Cang H; Labno A; Lu C; Yin X; Liu M; Gladden C; Liu Y; Zhang X Nature 2011, 469, 385–388. [PubMed: 21248848]
(19). Huang B; Babcock H; Zhuang X Cell 2010, 143, 1047–1058. [PubMed: 21168201]
(20). Zürner A; Kirstein J; Döblinger M; Bräuchle C; Bein T Nature 2007, 450, 705–708. [PubMed: 18046407]
(21). Kirstein J; Platschek B; Jung C; Brown R; Bein T; Bräuchle C Nat. Mater 2007, 6, 303–310. [PubMed: 17351614]
(22). Hell SW; Wichmann J Opt. Lett 1994, 19, 780–782. [PubMed: 19844443]
(23). Gustafsson MGL Journal of Microscopy 2000, 198, 82–87. [PubMed: 10810003]
(24). Rust MJ; Bates M; Zhuang X Nat. Methods 2006, 3, 793–796. [PubMed: 16896339]
(25). Hess ST; Girirajan TPK; Mason MD Biophys. J 2006, 91, 4258–4272. [PubMed: 16980368]
(26). Kim D-N; Kilchherr F; Dietz H; Bathe M Nucleic Acids Res. 2012, 40, 2862–2868. [PubMed: 22156372]
(27). Thompson RE; Larson DR; Webb WW Biophys. J 2002, 82, 2775–2783. [PubMed: 11964263]
(28). Li Z; Liu M; Wang L; Nangreave J; Yan H; Liu YJ Am. Chem. Soc 2010, 132, 13545–13552.
(29). Li Z; Wang L; Yan H; Liu Y Langmuir 2011, 28, 1959–1965. [PubMed: 22126326]
(30). Burge S; Parkinson GN; Hazel P; Todd AK; Neidle S Nucleic Acids Res. 2006, 34, 5402–5415. [PubMed: 17012276]
(31). Michelotti N; Johnson-Buck A; Manzo AJ; Walter NG Wiley Interdiscip. Rev.: Nanomed. Nanobiotechnol 2012, 4, 139–152. [PubMed: 22131292]
(32). Nangreave J; Han D; Liu Y; Yan H Curr. Opin. Chem. Biol 2010, 14, 608–615. [PubMed: 20643573]

Author Manuscript
Author Manuscript
Author Manuscript
Author Manuscript

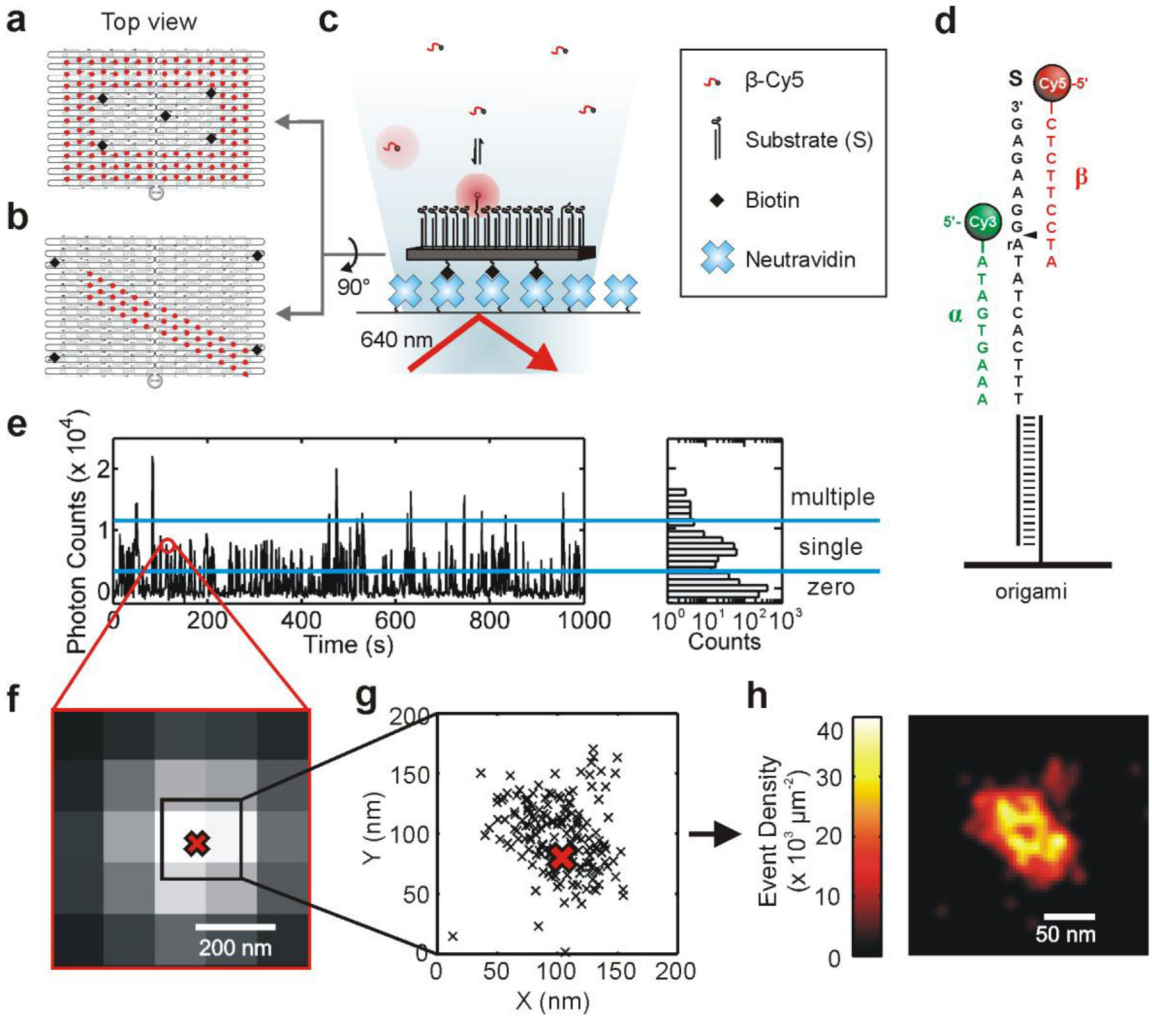

Figure 1.

Origami tile designs used in this study: (a) rectangular origami **R** bearing 126 substrates (red circles) and 5 biotin molecules (black diamonds) for immobilization on a NeutrAvidin-coated microscope slide; and (b) linear origami **L** bearing 42 substrates and 4 biotin molecules. Substrates and biotins are displayed on opposite faces of the tile. (c) Scheme for PAINT experiments. DNA origami were immobilized on a NeutrAvidin-coated fused silica slide on a TIRF microscope *via* multiple biotin-NeutrAvidin interactions. Imaging occurred in the presence of single-stranded DNA probes that were fluorescently labeled at their 5′-end. As probes bind reversibly to the substrates on the origami tile, they enter the evanescent field of excitation light and are localized. (d) Sequences of the substrate (S) and fluorescently labeled PAINT probes **α-Cy3** and **β-Cy5**. In some experiments, only **β-Cy5** was used; in others, **β** was labeled with Cy3 and **α** was labeled with Cy5. **S** contains an RNA base (rA) to allow for enzymatic cleavage at the site indicated by the black triangle. (e) Fluorescence intensity time trace and histogram showing repeated binding of **β-Cy5** to a single **R** origami tile. Only binding events with intensity between the two horizontal blue lines were used in the reconstruction, as these have a high probability of originating from individual **β-Cy5** molecules (rather than ≥ 2 bound simultaneously). For ease of viewing,

Author Manuscript Author Manuscript Author Manuscript Author Manuscript

only 1,000 s are shown from a 3,000-s experiment. (f) Wide-field diffraction-limited fluorescence image of the **β-Cy5** binding event circled in (e). The intensity profile is fit with a 2-D Gaussian function to localize the binding event (red X). (g) Coordinates of 174 localizations of **β-Cy5** binding PAINT reconstruction of an **R** origami. The red X corresponds to the localization of the binding event shown in (f). (h) PAINT reconstruction of the origami shown in (g). Each experiment yielded reconstructions for ~20-100 origami.

Author Manuscript Author Manuscript Author Manuscript Author Manuscript

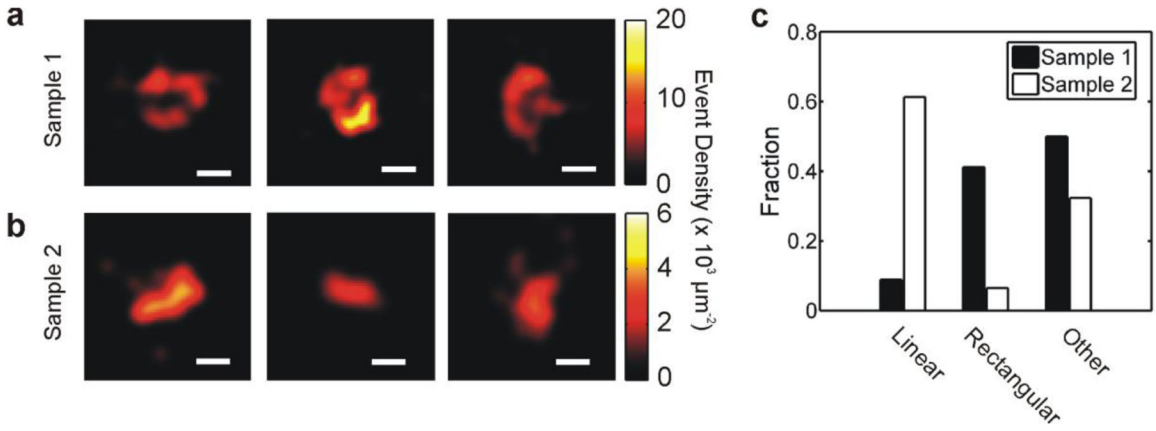

Figure 2.

One-color PAINT reconstructions of **R** (a) and **L** (b) origami tiles imaged in the presence of 10 nM **β-Cy5** with 20-60 binding events per tile. Scale bars: 50 nm. (c) Results from a blind experiment in which two origami samples of unknown identity (either **L** or **R**) were imaged in the presence of 10 nM **β-Cy5** and classified according to their morphology: linear (e.g. Figure 2b), rectangular (e.g., Figure 2a), or other (42 and 27 origami were examined from samples 1 and 2, respectively). The "other" category likely included malformed origami tiles, aggregates of multiple origami, or origami with spatially heterogeneous binding of **β-Cy5** (see Figure 4). Samples 1 and 2 were correctly identified as **R** and **L**, respectively.

Author Manuscript Author Manuscript Author Manuscript Author Manuscript

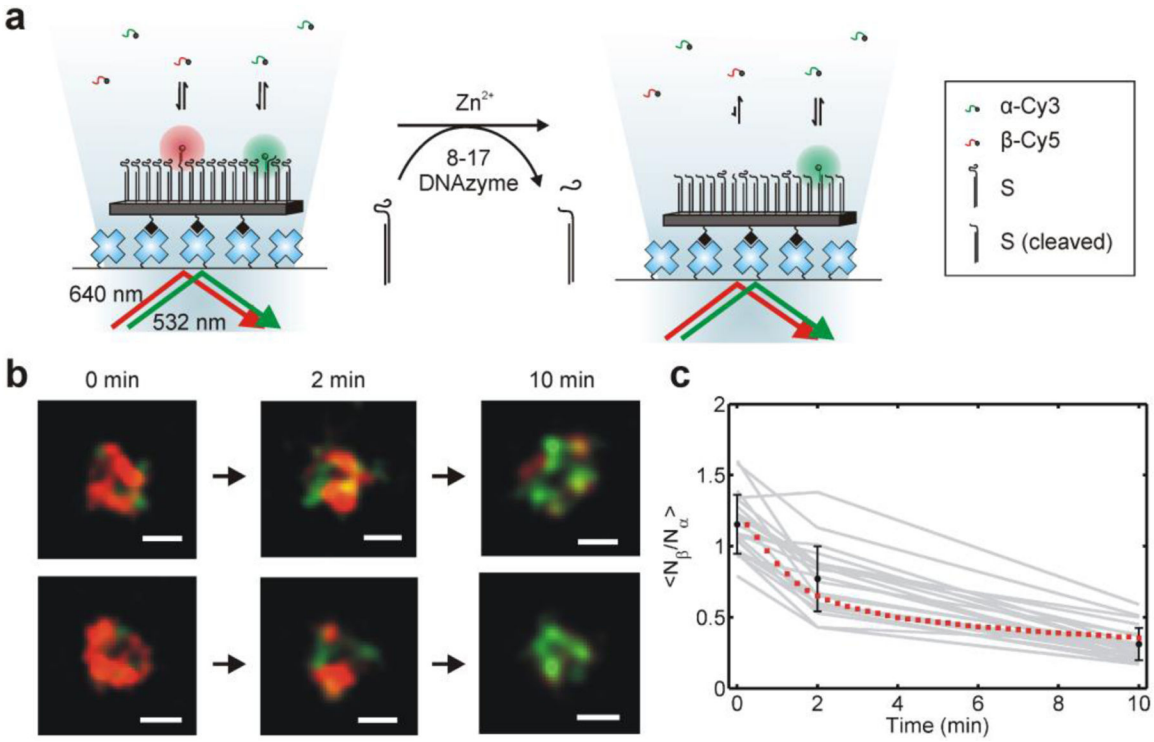

Figure 3.

(a) Experiment for monitoring chemical changes by two-color PAINT. **R** origami tiles were imaged in the presence of 10 nM each of **α-Cy3** and **β-Cy5**. Incubation with 1 μM 8-17 deoxyribozyme (DNAzyme) and 1 mM Zn^{2+} results in the cleavage of **S**. The cleavage product can bind probe **α**, but not probe **β**, resulting in a change in the PAINT readout. (b) Two-color reconstructions of three individual **R** origami tiles after 0, 2, or 10 min total incubation with 8-17 DNAzyme and Zn^{2+} (**α-Cy3**, green; **β-Cy5**, red, scale bars 50 nm). (c) Mean ratio of **β** binding events to **α** binding events for 21 **R** origami after 0, 2, or 10 min total incubation with 1 μM 8-17 DNAzyme and 1 mM $ZnSO_4$ (black circles, error bars 1 s.d.). The time courses for 21 individual origami tiles are also shown (gray lines). An ensemble time course for the cleavage of substrate on R origami under identical conditions, normalized to the initial value of $<N_\beta/N_\alpha>$, is shown for comparison (red squares, Figure S3).

Author Manuscript Author Manuscript Author Manuscript Author Manuscript

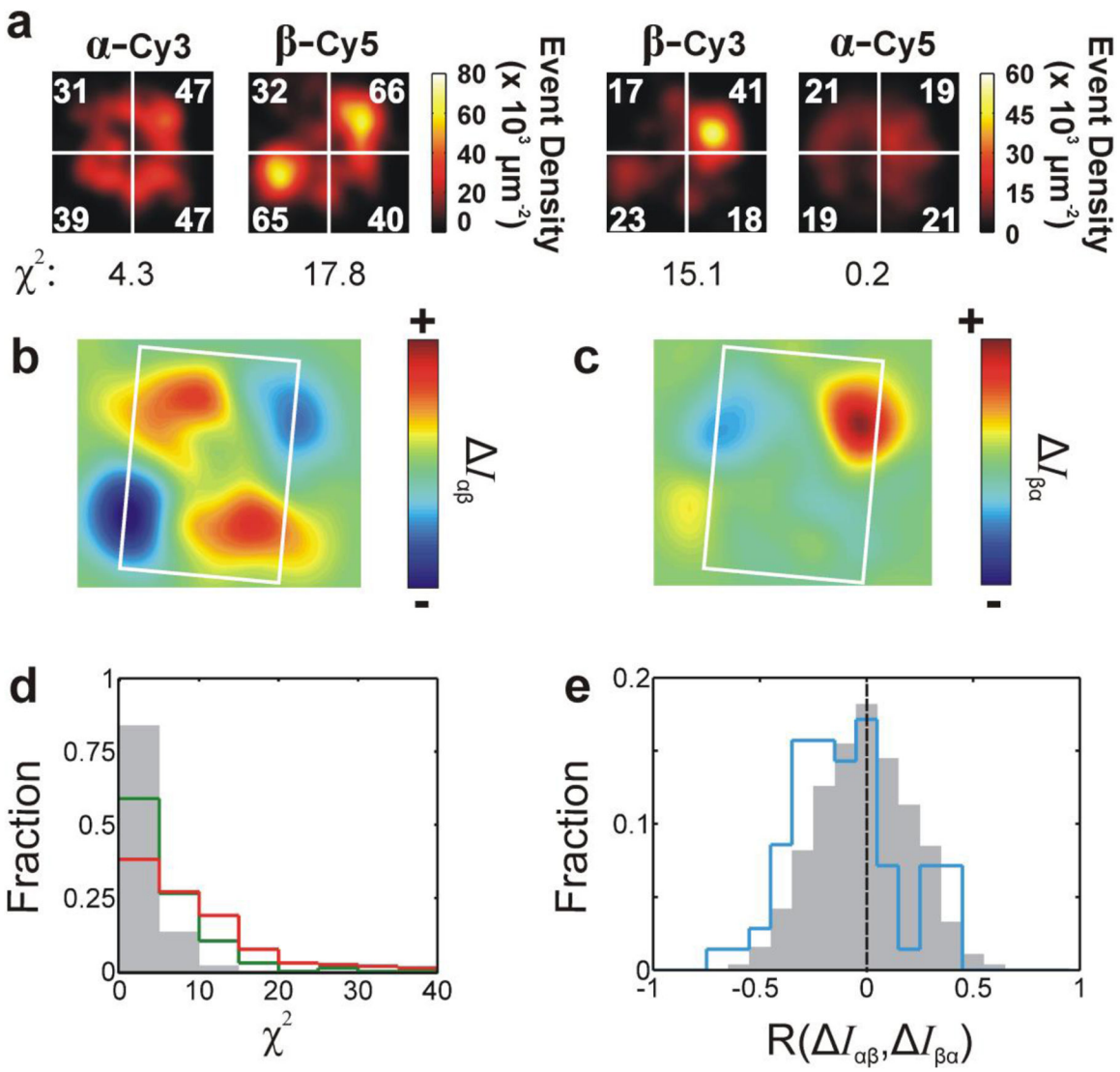

Figure 4.

(a) DNA-PAINT reconstructions of the same **R** origami tile using two different sets of probes: **α-Cy3** + **β-Cy5**, and **β-Cy3** + **α-Cy5**, and quantification of binding uniformity by chi-squared analysis of the distribution of binding events between origami quadrants. The number of binding events observed in a 60-min period is indicated in each quadrant. The distributions of **α-Cy3** and **α-Cy5** binding can be explained by a homogeneous model, while that of **β-Cy5** and **β-Cy3** cannot (df = 3, $P < 0.001$). Reconstructions are 125 × 125 nm^2. (b), (c) Intensity difference maps, calculated by subtracting the Cy5 reconstruction from the Cy3 reconstruction, for the origami tile shown in (a) as imaged by the two probe sets. White rectangular outlines depict typical origami dimensions as measured by AFM (60 x 90 nm). In (b), $\Delta I_{\alpha\beta} = I_{\alpha\text{-}Cy3} - I_{\beta\text{-}Cy5}$, while in (c), $\Delta I_{\beta\alpha} = I_{\beta\text{-}Cy3} - I_{\alpha\text{-}Cy5}$. The difference maps in (b) and (c) have a correlation coefficient $R = -0.67$. (d) Histograms of χ^2 for the binding distributions of probes **α** (green line) and **β** (red line) to 173 **R** origami, as compared to the distribution predicted from 1,000 simulated **R** origami (gray shaded region). (e) Histogram of correlation coefficients between difference maps $\Delta I_{\alpha\beta}$ and $\Delta I_{\beta\alpha}$ for 70 **R** origami tiles

Author Manuscript Author Manuscript Author Manuscript Author Manuscript

(blue line; $\mu = -0.10$, s.e.m. = 0.03) as compared to the results from 1,000 simulated tiles (gray shaded region; $\mu = -0.008$, s.e.m. = 0.008). The black dashed line indicates the mean value of the simulated distribution. The experimental distribution is significantly skewed toward negative values compared to the simulated distribution ($t(69) = 3.1$, two-tailed $P = 0.003$).

Author Manuscript Author Manuscript Author Manuscript Author Manuscript

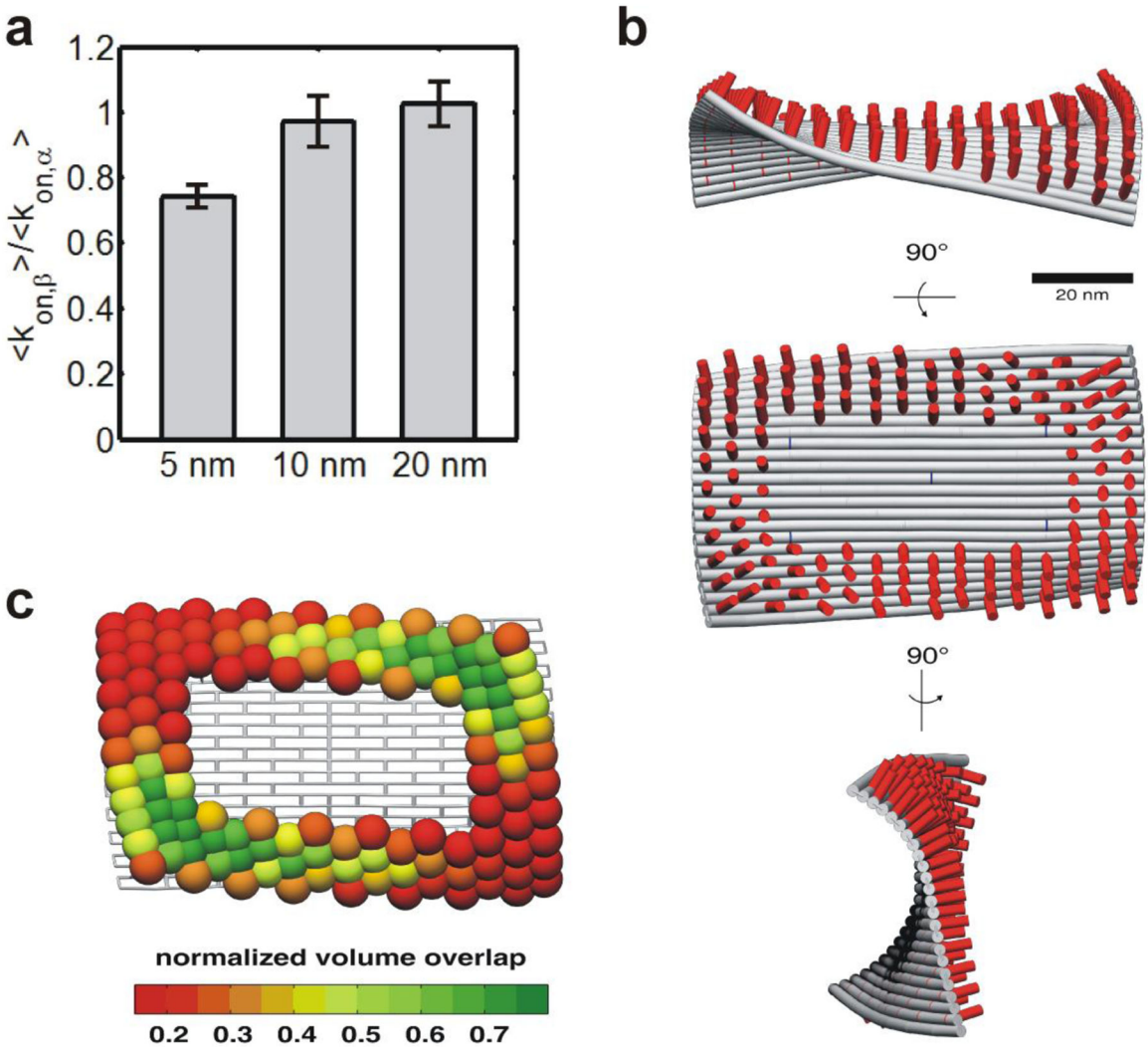

Figure 5.

(a) Relative association rate constants of **α-Cy3** and **β-Cy5** to origami with approximate distances of 5, 10, or 20 nm between adjacent **S** strands. Error bars: 1 s.e.m. (b) Three-dimensional solution structure of **R** origami tile predicted by CanDo with constrained biotin positions (see Supporting Methods). Red cylinders represent **S** positions. (c) Normalized effective volume overlap of neighboring free **S** strands on **R** origami based on the CanDo structural model in panel (b).